THE JOURNAL OF
PHYSICAL CHEMISTRY C

Article

pubs.acs.org/JPCC

Exciton Lifetime Broadening and Distribution Profiles of PbS Colloidal Quantum Dot Thin Films Using Frequency- and Temperature-Scanned Photocarrier Radiometry

Jing Wang,[†,‡] Andreas Mandelis,*[,†,§] Alexander Melnikov,[†] Sjoerd Hoogland,[§] and Edward H. Sargent[§]

[†]Center for Advanced Diffusion-Wave Technologies (CADIFT), Department of Mechanical and Industrial Engineering, University of Toronto, Toronto, Ontario M5S 3G8, Canada

[‡]School of Optoelectronic Information, University of Electronic Science and Technology of China, Chengdu, Sichuan, 610054, China

[§]Edward S. Rogers Sr. Department of Electrical and Computer Engineering, University of Toronto, Toronto, Ontario M5S 3G4, Canada

Ⓢ *Supporting Information*

ABSTRACT: Photocarrier radiometry (PCR) has been applied to PbS colloidal quantum dot (CQD) thin films for the absolute measurement of emission lifetimes. Continuous and discrete models describing lifetime distribution have been developed. The former yields homogeneous and inhomogeneous Voigt lifetime broadening. The latter comprises two models: one is based on direct *ad hoc* fits to PCR amplitude and phase data, reconstructing a superposition of multiple independent lifetime line spectra; the other is a variational method developed to invert simultaneous integral equations in the lifetime distribution function (spectrum) and involves similar fits to the PCR in-phase and quadrature signal channels to reconstruct the lifetime spectrum. A PCR theory with a rate equation model taking into account the lowest 1S−1S exciton state splitting and multiphonon-assisted carrier trapping to states outside a PbS QD was also developed. For noninteracting (uncoupled) CQDs, longitudinal optical (LO) phonon−exciton interactions limit the radiative lifetime and luminescence photon flux throughout the entire 100−300 K temperature range. For interacting (coupled) CQDs, variational and *ad hoc* lifetime line spectra exhibit similar mechanisms to uncoupled CQDs with the important addition of direct exciton-to-exciton transitions in the form of efficient transport (hopping, tunneling, or FRET) at all temperatures, which result in de-excitation dynamics dominated by radiative emission channels.

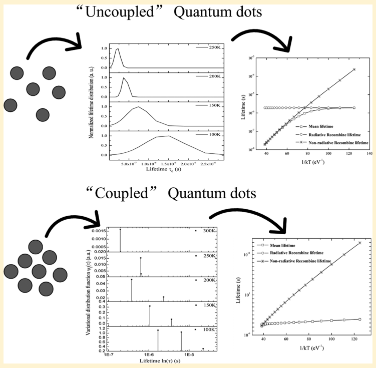

1. INTRODUCTION

Lead-salt (PbS, PbSe, and PbTe) colloidal quantum dots (CQD) have been successfully employed as active components in electronic and optoelectronic devices such as photodetectors,[1,2] light-emitting diodes,[3,4] and solar cells.[5,6] Currently, the most efficient CQD solar cells reported by Maraghechi et al.[7] with power conversion efficiencies of 8% employ the depleted-heterojunction architecture consisting of a p-type PbS CQD layer coating on a transparent n-type metal oxide.[8] Studies of lead-salt QDs have been carried out for several decades and still attract a growing number of investigations from both fundamental and applied points of view. By adjustment of composition, size, shape, monodispersity, capping ligand, and surface chemistry, as well as the degree of super lattice order in the films, electronic and optical properties become tunable. Various tunability mechanisms have been found and studied during the past decade. For example, for carrier delocalization, Mentzel et al.[9] measured the current of PbSe nanocrystal (NC) array-based field-effect transistors as a function of source-drain voltage, gate voltage, and temperature, while Kang et al.[10] studied the size- and temperature-dependent charge transport in PbSe NC thin films and found that the electron transport occurred at higher temperatures for films with smaller particles. Clark et al.[11] studied Förster resonant energy transfer (FRET) of carriers between smaller and bigger sizes of PbS QDs with continuous wave and time-resolved fluorescence experiments. These authors established that there is a size dependence of fluorescence emission lifetimes in PbS quantum dots. Subsequently, Chen et al.[12] studied size-dependent radiative emissions from PbS quantum dots embedded in a Nafion membrane using time-resolved photoluminescence (PL) decay and reported decreasing decay time with increasing QD size, possibly a result of less effective dielectric screening with larger QDs.[13] A transient PL lifetime proportionality to polyacrylamide polymer-film-embedded PbS nanoparticle diameter has also been observed by Lifshitz et al.,[14] an opposite trend to that found by Chen et al.[12] Besides FRET, transport mechanisms explored in QD films include variable-range hopping (VRH) as reported by Yu et al.[15] and Romero and Drndic[16] for PbSe QDs and tunneling between

Received: July 22, 2013
Revised: October 2, 2013
Published: October 4, 2013

dx.doi.org/10.1021/jp407228k | *J. Phys. Chem. C* 2013, 117, 23333−23348

adjacent CQDs studied by Talapin et al.[17] Multiple exciton generation (MEG) and carrier relaxation processes have also been studied by Ellingson et al.[18] and Istrate et al.[19] Carriers trapped in trap states play a pertinent role in charge transport as reported by Sargent et al.[20] and Gao and Johnson.[21] Nevertheless, while the details of the exciton relaxation mechanism(s) in PbS CQDs are essential for an understanding of the optical-to-electronic energy conversion mechanism on which devices such as QD solar cells depend, the physical picture is far from clear because PL lifetime measurement methodologies to-date have not been accurate enough to determine the distribution of lifetimes. Although dc (or continuous) PL is a commonly used tool for investigating QD photophysics, it is not suitable for measuring dynamic processes such as exciton decays. Time-resolved PL has been used for the purpose of measuring relaxation lifetimes in PbS QDs at various temperatures.[22,23] However, several major issues arise with this modality: excessive noise due to the broad bandwidth of fast detectors required to capture the transient, especially at long times of the PL transient (tens of microseconds), thereby yielding poor lifetime accuracy[23] and the nonexponential character of the decay, which makes the use of deconvolution algorithms imprecise and resulting lifetimes poorly resolved and only under the assumption of discrete lifetimes. The development of reliable physical models of QD excited-state interactions as a function of parameters like ambient temperature and QD and trap densities can only be accomplished if the foregoing limitations on lifetime accuracy and precision and resolution can be overcome.

Photocarrier radiometry (PCR)[24−28] is a dynamic spectrally integrated (in the present case) frequency-domain PL modality, the spectral bandwidth of which is gated to eliminate thermal-infrared photon contributions resulting from radiative emission reabsorption and nonradiative conversion. PCR can yield quantitative information about relaxation lifetime distributions and their radiative and nonradiative components associated with intra-QD and inter-QD excited state decay processes with accuracy and precision superior to time-resolved PL due to its intrinsically high signal-to-noise ratio (SNR) based on narrowband lock-in demodulation. The replacement of time-domain signal deconvolution requirements with two simultaneous integral equations in the frequency domain yielding theoretically identical lifetime spectra enhances measurement reliability and accuracy. Coupled with a physical relaxation model, PCR can allow the formulation of an inverse problem approach to reconstructing lifetime distributions (spectra) as a function of temperature, thereby probing various intra- and inter-QD relaxation processes through their respective lifetimes. This process can successfully link definitive physical models to the decay rates of exciton relaxation mechanisms.

In this work, we develop a frequency-domain exciton de-excitation and carrier trapping theory through a modification of the temperature-dependent time-resolved PL quantum dot model by Gaponenko et al.[23] to address the problem of relaxation time distribution extraction and potential physical origins of the associated exciton relaxation mechanisms in CQD thin films currently used for the fabrication of heterojunction solar cells.[8] The frequency-domain theory has allowed the decoupling of exciton radiative and nonradiative lifetime expressions without the need for PL signal normalization and allowed for the concept of relaxation time broadening. Continuous and discrete approaches to the lifetime reconstruction (inverse) problem at fixed temperature are introduced between 100 and 300 K, and the derived relaxation time distributions (spectra) are used with the PCR theory to study CQD exciton dynamics and inter-QD exciton transport processes involved in two PbS CQD thin films with different dot-to-dot spacing.

2. THEORETICAL METHODS

2.1. Exciton Lifetime Distributions (Spectra) In Photo-excited PbS Quantum Dot Systems.

2.1.1. QD Size-Distribution-Related Continuous Gaussian Lifetime Distribution. Clark et al.[11] spectrally resolved fluorescence decays of close-packed PbS QDs dispersed in tetrachloroethylene, chloroform, or hexane solvents and in the dry state in films photoexcited at 920 and 960 nm. They observed that different fluorescence wavelengths are characterized by different decay times which, in turn, were associated with FRET between QDs of smaller and larger sizes, given the excitonic quantum energy level dependence on quantum dot size. They concluded that different wavelengths are emitted by quantum dots of continuous size distributions and different lifetimes. Similar conclusions were reached by Chen et al.[12] with regard to PbS QDs in a Nafion membrane and by Lifschitz et al.[14] This latter group reported fluorescence emission trends consistent with smaller size QDs emitting radiation of shorter lifetime, but the trends with emitted wavelength were not consistent. In general, a continuous distribution of sizes is expected in any QD sample, albeit narrow or wide even within a nominally single size quantum dot assembly. It is also reasonable to assume a correspondence between size and decay lifetime upon energy exchange between smaller dots (higher exciton energy levels) and larger dots (lower energy levels).[11,29] Given the random distribution of QD sizes within a solid film, a Gaussian exciton relaxation time distribution mirroring the random size distribution can be described as

$$f(\tau) = f_0\ \mathrm{e}^{-[(\tau-\tau_0)/\Delta\tau]^2} \tag{1}$$

Here τ_0 is the most probable relaxation lifetime, and $\Delta\tau$ is the lifetime spread (line width). A time-domain approach to photoluminescence decay kinetics from carriers trapped in exciton states can be represented as[23]

$$I(t) = \int_{\tau_{\min}}^{\tau_{\max}} f(\tau)\ \mathrm{e}^{-t/\tau}\ \mathrm{d}\tau \tag{2}$$

The PCR frequency response of a PbS colloidal QD system can be obtained from the Fourier transform:

$$F(\omega) = \int_0^\infty I(t)\ \mathrm{e}^{-i\omega t}\ \mathrm{d}t \simeq \int_0^\infty \mathrm{d}t \int_{-\infty}^\infty f(\tau)\ \mathrm{e}^{-t/\tau - i\omega t}\ \mathrm{d}\tau \tag{3}$$

where a continuous or discrete but physically finite distribution of lifetimes allows the truncated lower and upper limits of the lifetime integral (eq 2) to be approximated by the full range of possible lifetimes. It is straightforward to show that

$$F(\omega) = \int_0^\infty \frac{\tau f(\tau)\ \mathrm{d}\tau}{1 + i\omega\tau} \tag{4}$$

Here, $f(\tau)$ is the (unknown) lifetime distribution function and the range of lifetimes is physically limited to positive values. In the case of a Gaussian lifetime distribution

$$F(\omega) = f_0 \int_0^\infty \frac{\tau\ \mathrm{e}^{-[(\tau-\tau_0)/\Delta\tau]^2}\ \mathrm{d}\tau}{1 + i\omega\tau} \tag{5}$$

This is the desired frequency response when the lifetime spectrum is broadened due to QD excited state energy transfer. Such a mechanism is associated with the variable relaxation processes due to the random distribution of the QD sizes within a solid film. The complex integral (eq 5) can be separated into real and imaginary parts:

$$F(\omega) = A(\omega) + iB(\omega) \tag{6}$$

where

$$A(\omega) \equiv f_0 \int_0^{\infty} \frac{\tau\, e^{-[(\tau-\tau_0)/\Delta\tau]^2}\, d\tau}{1+\omega^2\tau^2} \tag{7a}$$

$$B(\omega) \equiv -f_0\omega \int_0^{\infty} \frac{\tau^2\, e^{-[(\tau-\tau_0)/\Delta\tau]^2}\, d\tau}{1+\omega^2\tau^2} \tag{7b}$$

These integrals belong to a category of generalized Voigt functions that typically arise in the case of convolution between homogeneous and inhomogeneous broadening in gas phase spectroscopy.[30] In the context of QDs, this gives rise to the concept of inhomogeneous "lifetime broadening" involving nanoparticle size, exciton scattering, multienergetic trap states, and resonance mechanisms. Proper Voigt integrals have $-\infty$ as the lower limit, which was the case here before the negative τ value range was truncated out on physical grounds. Computationally, it also turns out that the contribution of the negative τ value range to both integrals (eqs 7a and 7b) is negligible.

2.1.2. QD Size-Distribution-Related Discrete Lifetime Distributions. 2.1.2.1. Hierarchically Constrained Multiple Relaxation Dynamics. The relaxation time distribution, eq 2, in its generalized form

$$I(t) = \int_0^{\infty} f(\tau)\, e^{-t/\tau}\, d\tau \tag{8}$$

is a statement that there may be appreciable QD system relaxation correlations on several time scales, which raises the possibility of a statistical distribution of relaxation times across several degrees of freedom. This concept has been applied to atomic systems undergoing glassy relaxation and has been shown[31] to lead naturally to the Kohlrausch anomalous relaxation law,[32] also known as the stretched exponential

$$I(t) = I_0 \exp[-(t/\tau)^{\beta}], \quad 0 \le \beta \le 1 \tag{9}$$

This law has been shown to hold in electronic systems as well, such as optoelectronic semiconductors, specifically in describing defect state dynamics in semi-insulating GaAs.[28] Its physical meaning lies in the hierarchically constrained dynamics of systems exhibiting the law, so that each degree of freedom relaxes to equilibrium in a serial manner, not in independent parallel relaxations, following the attainment of prior degrees of freedom such as hierarchical (serial) carrier emission from defect states or radiative recombination. A number of authors have used the stretched exponential time decay of the PL signal as a model for exciton hopping in combination with a nanocrystal (NC) Gaussian size distribution. They have associated the mostly empirical experimental validity of eq 9 with energetically nonisolated nanocrystals exhibiting exciton interactions[33−35] or even with electron−hole pair recombinations within an ensemble averaged distance.[14] Most of these treatments did not attach any physical meaning to the time constant τ in the stretched exponential used either alone, in a summation with additional stretched exponentials,[14] or in *ad hoc* combination with other transient functions[36] so as to fit the transient PL decay curves empirically. All relaxation time constants led to the calculation of an average relaxation time, thereby losing the physical picture of distribution.[14,23]

2.1.2.2. Ad Hoc Discrete Lifetime Distributions. In retaining the essence of the lifetime distribution of eq 2 or its generalization, eq 8, the integral can be approximated in an *ad hoc* manner with a superposition of discrete single-exponential-decay profiles. Then eqs 2 and 4 can be written, respectively, as

$$I(t) = \int_{\tau_{\min}}^{\tau_{\max}} f(\tau)\, e^{-t/\tau}\, d\tau \approx \sum_{j=1}^{n} f_j \exp(-t/\tau_j) \tag{10}$$

and

$$F(\omega) \approx \sum_{j=1}^{n} \left(\frac{f_j\tau_j}{1+i\omega\tau_j} \right) \tag{11}$$

Where n is the number of the effective multilifetime components and f_j has the meaning of a weighing constant. The mean decay lifetime can be calculated as[23]

$$\overline{\tau} = \frac{(\sum_{i=1}^{n} f_i\tau_i^2)}{(\sum_{i=1}^{n} f_i\tau_i)} \tag{12}$$

This approach provides the simplest discrete lifetime reconstruction methodology when eq 11 is best-fitted to frequency-domain PCR amplitude and phase data. However, the extent of its correctness and accuracy is unknown because the approximation (eq 10) can be readily justified neither on mathematical nor on physical grounds. Therefore, there is a strong possibility of the appearance of artifacts upon inversion of eq 11 in reconstructing the lifetime distribution (spectrum) on a time axis. A rigorous approach can be introduced based on variational inversion of the frequency-domain counterpart, eq 4, of the generalized relaxation time distribution, eq 8.

2.1.2.3. Variational Inverse Exciton Relaxation Time Distribution Problem. Equation 4 can be considered as an integral equation, where $f(\tau)$ is the (unknown) lifetime distribution function and $F(\omega)$ is a known function, a frequency response that can be measured experimentally. $f(\tau)$ can be extracted using inversion methods for integral equations. Here only positive lifetimes have been considered. When resolved into its real and imaginary parts, eq 4 yields

$$\mathrm{Re}[F(\omega)] \equiv F_R(\omega) = \int_0^{\infty} \left[\frac{1}{1+(\omega\tau)^2} \right] \tau f(\tau)\, d\tau; \quad 0 \le \omega < \infty \tag{13}$$

$$\mathrm{Im}[F(\omega)] \equiv F_I(\omega) = -\int_0^{\infty} \left[\frac{\omega\tau}{1+(\omega\tau)^2} \right] \tau f(\tau)\, d\tau; \quad 0 \le \omega < \infty \tag{14}$$

These are two simultaneous Fredholm integral equations, each of which can be considered an inverse problem for $f(\tau)$ using PCR signal real and imaginary parts. The above equations can be written in the forms

$$\int_0^{\infty} K_R(\omega\tau)\Psi_R(\tau)\, d\tau = F_R(\omega); \quad 0 \le \omega < \infty \tag{15a}$$

with the symmetric kernel

$$K_{\mathrm{R}}(\omega\tau) = \frac{1}{1 + (\omega\tau)^2} \tag{15b}$$

and

$$\int_0^\infty K_{\mathrm{I}}(\omega\tau)\Psi_{\mathrm{I}}(\tau)\,\mathrm{d}\tau = F_{\mathrm{I}}(\omega); \qquad 0 \le \omega < \infty \tag{16a}$$

with the (also) symmetric kernel

$$K_{\mathrm{I}}(\omega\tau) = -\frac{\omega\tau}{1 + (\omega\tau)^2} \tag{16b}$$

2.1.2.3.1. Inverse Problem: Real Part. Assuming the existence of multiple (n) Gaussian broadened time constants in the system, the variational solution function is (Supporting Information 1, Appendix, eq A9)

$$\Psi_{\mathrm{R}}(\tau) = \sum_{i=1}^{n} \alpha_i \tau\, \mathrm{e}^{-[(\tau-\tau_i)/\Delta\tau_i]^2} \tag{17}$$

The square matrix expression that solves for the variational coefficients α_i, eq A13, is

$$\sum_{m=1}^{n} \alpha_m H_{\mathrm{R},im}(\tau_m, \omega_i; \Delta\tau_m, \Delta\omega_i) = S_{\mathrm{R}i}(\omega_i, \Delta\omega_i);$$

$$1 \le m \le n, \qquad 1 \le i \le n \tag{18}$$

where three integrals are involved(Supporting Information 1, Appendix, eqs A12 and A14):

$$A_m(\omega; \tau_m, \Delta\tau_m) \equiv \int_0^\infty \frac{\mathrm{e}^{-[(\tau-\tau_m)/\Delta\tau_m]^2}\tau\,\mathrm{d}\tau}{1 + (\omega\tau)^2}$$

$$\text{(Voigt integral)} \tag{19}$$

$$H_{\mathrm{R},kj}(\tau_j, \omega_k; \Delta\tau_j, \Delta\omega_k) = \int_0^\infty A_j(\omega; \tau_j, \Delta\tau_j)\,\mathrm{e}^{-[(\omega-\omega_k)/\Delta\omega_k]^2}\omega\,\mathrm{d}\omega \tag{20}$$

and

$$S_{\mathrm{R}i}(\omega_i, \Delta\omega_i) = \int_0^\infty F_{\mathrm{R}}(\omega)\,\mathrm{e}^{-[(\omega-\omega_i)/\Delta\omega_i]^2}\omega\,\mathrm{d}\omega \tag{21}$$

with ω_i and $\Delta\omega_i$ formally representing the peak value and spread (line width) of the Fourier transform of the lifetime distribution: $\omega_i = 2\pi/\tau_i$; $\Delta\omega_i = 2\pi/\Delta\tau_i$. In practice, these values are determined from the frequency spacing of experimental data.

2.1.2.3.2. Inverse Problem: Imaginary Part. The variational function for the imaginary integral equation can be written as

$$\Psi_{\mathrm{I}}(\tau) = \sum_{i=1}^{n} \beta_i \tau\, \mathrm{e}^{-[(\tau-\tau_i)/\Delta\tau_i]^2} \tag{22}$$

and the square matrix expression that solves for the variational coefficients β_i is

$$\sum_{m=1}^{n} \beta_m H_{\mathrm{I},im}(\tau_m, \omega_i; \Delta\tau_m, \Delta\omega_i) = S_{\mathrm{I}i}(\omega_i, \Delta\omega_i);$$

$$1 \le m \le n, \qquad 1 \le i \le n \tag{23}$$

where, again, the following three integrals are involved (Supporting Information 1, Appendix, eqs A12 and A14):

$$B_m(\omega; \tau_m, \Delta\tau_m) \equiv \int_0^\infty \frac{\mathrm{e}^{-[(\tau-\tau_m)/\Delta\tau_m]^2}\tau^2\,\mathrm{d}\tau}{1 + (\omega\tau)^2}$$

$$\text{(modified Voigt integral)} \tag{24}$$

$$H_{\mathrm{I},kj}(\tau_j, \omega_k; \Delta\tau_j, \Delta\omega_k) = -\int_0^\infty B_j(\omega; \tau_j, \Delta\tau_j)\,\mathrm{e}^{-[(\omega-\omega_k)/\Delta\omega_k]^2}\omega^2\,\mathrm{d}\omega \tag{25}$$

$$S_{\mathrm{I}i}(\omega_i, \Delta\omega_i) = \int_0^\infty F_{\mathrm{I}}(\omega)\,\mathrm{e}^{-[(\omega-\omega_i)/\Delta\omega_i]^2}\omega\,\mathrm{d}\omega \tag{26}$$

2.1.2.3.3. Special Case a: Continuous Spectrum, n = 1. This case corresponds to a single broadened lifetime. Equation 18 gives for $n = 1$

$$\alpha_1 = \frac{\int_0^\infty F_{\mathrm{R}}(\omega)\,\mathrm{e}^{-[(\omega-\omega_1)/\Delta\omega_1]^2}\omega\,\mathrm{d}\omega}{\int_0^\infty A_1(\omega; \tau_1, \Delta\tau_1)\,\mathrm{e}^{-[(\omega-\omega_1)/\Delta\omega_1]^2}\omega\,\mathrm{d}\omega} \tag{27}$$

with

$$\Psi_{\mathrm{R}}(\tau) = \alpha_1\tau\,\mathrm{e}^{-[(\tau-\tau_1)/\Delta\tau_1]^2} \tag{28}$$

and

$$A_1(\omega; \tau_1, \Delta\tau_1) = \int_0^\infty \frac{\mathrm{e}^{-[(\tau-\tau_1)/\Delta\tau_1]^2}\tau\,\mathrm{d}\tau}{1 + (\omega\tau)^2} \tag{29}$$

For the imaginary part, eq 23 gives

$$\beta_1 = -\frac{\int_0^\infty F_{\mathrm{I}}(\omega)\,\mathrm{e}^{-[(\omega-\omega_1)/\Delta\omega_1]^2}\omega\,\mathrm{d}\omega}{\int_0^\infty B_1(\omega; \tau_1, \Delta\tau_1)\,\mathrm{e}^{-[(\omega-\omega_1)/\Delta\omega_1]^2}\omega^2\,\mathrm{d}\omega} \tag{30}$$

with

$$\Psi_{\mathrm{I}}(\tau) = \beta_1\tau\,\mathrm{e}^{-[(\tau-\tau_1)/\Delta\tau_1]^2} \tag{31}$$

and

$$B_1(\omega; \tau_1, \Delta\tau_1) = \int_0^\infty \frac{\mathrm{e}^{-[(\tau-\tau_1)/\Delta\tau_1]^2}\tau^2\,\mathrm{d}\tau}{1 + (\omega\tau)^2} \tag{32}$$

2.1.2.3.4. Special Case b: Discrete Lifetime Multicomponent Spectrum. In the limit where the τ distribution consists of sharply peaked components ($\Delta\tau \ll \tau_1$ and $\Delta\omega \ll \omega_1$), we can set

$$\mathrm{e}^{-[(\tau-\tau_i)/\Delta\tau_i]^2} \to \delta(\tau - \tau_i); \qquad \mathrm{e}^{-[(\omega-\omega_i)/\Delta\omega_i]^2} \to \delta(\omega - \omega_i) \tag{33}$$

so that the variational solutions, eqs 17 and 22, become:

$$\Psi_{\mathrm{R}}(\tau) = \sum_{i=1}^{n} \alpha_i\tau\delta(\tau - \tau_i) \equiv \sum_{i=1}^{n} \alpha_i\Psi_{\mathrm{R}i}(\tau) \tag{34}$$

$$\Psi_{\mathrm{I}}(\tau) = \sum_{i=1}^{n} \beta_i\tau\delta(\tau - \tau_i) \equiv \sum_{i=1}^{n} \beta_i\Psi_{\mathrm{I}i}(\tau) \tag{35}$$

Equation 18 can be written as

$$\sum_{m=1}^{n} \frac{\alpha_m\tau_m}{1 + (\omega_i\tau_m)^2} = F_{\mathrm{R}}(\omega_i); \qquad 1 \le m \le n, \qquad 1 \le i \le n \tag{36}$$

This calls for a matrix inversion (Supporting Information 1, Appendix, eq A13):

$$\begin{pmatrix}\alpha_1\\ \alpha_2\\ \cdots\\ \alpha_n\end{pmatrix}\begin{bmatrix}H_{11} & H_{12} & \cdots & H_{1n}\\ H_{21} & H_{22} & \cdots & H_{2n}\\ \cdots & \cdots & \cdots & \cdots\\ H_{n1} & H_{n2} & \cdots & H_{nn}\end{bmatrix} = \begin{pmatrix}F_R(\omega_1)\\ F_R(\omega_2)\\ \cdots\\ F_R(\omega_n)\end{pmatrix} \tag{37}$$

where

$$H_{jk} = \frac{\tau_k}{1 + (\omega_j \tau_k)^2} \tag{38}$$

The thus calculated α_i can be used in eq 34 to build the discrete lifetime (line) spectrum from the real part of the frequency data (lock-in in-phase signal). Similarly, from the imaginary part, eq 23 becomes

$$-\sum_{m=1}^{n} \frac{\beta_m \omega_i \tau_m^{\ 2}}{1 + (\omega_i \tau_m)^2} = F_I(\omega_i) \tag{39}$$

In matrix form,

$$\begin{pmatrix}\beta_1\\ \beta_2\\ \cdots\\ \beta_n\end{pmatrix}\begin{bmatrix}L_{11} & L_{12} & \cdots & L_{1n}\\ L_{21} & L_{22} & \cdots & L_{2n}\\ \cdots & \cdots & \cdots & \cdots\\ L_{n1} & L_{n2} & \cdots & L_{nn}\end{bmatrix} = -\begin{pmatrix}F_I(\omega_1)\\ F_I(\omega_2)\\ \cdots\\ F_I(\omega_n)\end{pmatrix} \tag{40}$$

where

$$L_{jk} = \frac{\omega_j \tau_k^{\ 2}}{1 + (\omega_j \tau_k)^2} \tag{40a}$$

The thus calculated β_i can be used in eq 35 to build the discrete lifetime spectrum from the imaginary part of the frequency data (lock-in quadrature signal). The two spectra from real and imaginary parts are theoretically identical; however, in practice, there are differences by virtue of the nature of the two lock-in data channels.

2.2. Frequency-Domain Approach to PbS Colloidal Quantum Dot Exciton Relaxation Dynamics.

The dynamic system model involves exciton states split into a triplet "dark" and a higher energy singlet "bright" state at energies E_t and E_s, respectively, above the exciton ground state.[22] The two states have population $N_t(t)$ and $N_s(t)$, respectively. Physically, external optical excitation raises the exciton into some high virtual energy state from which the involved electron decays very rapidly (picoseconds) into the two lowest excited triplet and singlet states, which are also interacting with each other, Figure 1. From those two states, the electron comprising the exciton decays into the ground or a trap state through radiative and nonradiative pathways with corresponding singlet and triplet lifetimes τ_{Rs} and τ_{Rt} (radiative), and τ_{NRs} and τ_{NRt} (nonradiative). Aided by phonon interactions from the surrounding thermal bath at temperature T, excitons can transition to ground state nonradiatively either through crossing over into trap states of the surrounding matrix outside the core exciton or through surface states of the excitonic PbS nanoparticle itself. We assume[23] that it takes m-phonon emission in the triplet state and n-phonon emission in the singlet state for the electron to complete the nonradiative transition and decay to the ground state through that pathway. Given that the relaxation time for the 1S−1S exciton fine structure states in PbS quantum dots has been measured to be <1 ps,[37] the narrowly separated split-state populations are assumed to be at thermal equilibrium in the microsecond time scale exhibited by PbS nanoparticles.

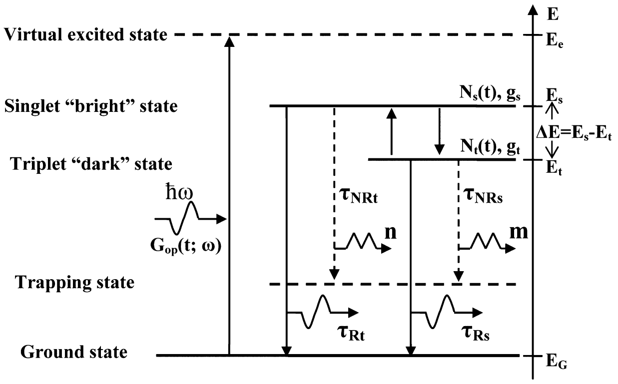

Figure 1. Excited state manifold of PbS exciton in the singlet−triplet energy range. Photon emission: sine wave arrows indicate radiative emission processes. Phonon emission: sawtooth arrows indicate nonradiative decay processes in the presence of photocarrier exciton traps.

For harmonically modulated optical excitation, the rate equations corresponding to the excited-state manifold of Figure 1 are

$$\frac{dN(t)}{dt} = G_{op}(t;\,\omega) - \left(\frac{1}{\tau_{Rt}} + \frac{1}{\tau_{NRt}}\right)N_t(t) - \left(\frac{1}{\tau_{Rs}} + \frac{1}{\tau_{NRs}}\right)N_s(t) \tag{41a}$$

$$\frac{N_s(t)}{N_t(t)} = \left(\frac{g_s}{g_t}\right)e^{-\Delta E/k_BT} \tag{41b}$$

with

$$N_s(t) + N_t(t) = N(t) \tag{41c}$$

Here $\Delta E = E_s - E_t$; g_j stands for the degeneracy factor of electrons in state j. The exciton generation rate using a laser beam modulated at angular frequency ω is

$$G_{op}(t;\,\omega) = \frac{1}{2}G_0(1 + e^{i\omega t}) \tag{42}$$

where G_0 is the optical excitation rate amplitude [cm^{-3} s^{-1}]. The two nonradiative lifetimes are a function of temperature through their dependence on phonon populations or on trap/surface states with temperature-dependent occupation probabilities:[23]

$$\begin{aligned}\tau_{NRs}(T) &= \tau_{NR0}[\exp(E_p/k_BT) - 1]^n\\ \tau_{NRt}(T) &= \tau_{NR0}[\exp(E_p/k_BT) - 1]^m\end{aligned} \tag{43}$$

where τ_{NR0} is a time constant for thermal (nonradiative) decay of excitonic electrons into a trap or surface state via emission of n or m phonons ($m > n$). E_p is the longitudinal optical (LO)-phonon energy, which in PbS is equal to 26.6 meV.[38] The solution of the system of eqs 41 with modulated population

$$N_J(\omega;\,t) = \frac{1}{2}n_J(\omega)(1 + e^{i\omega t});\qquad J = t,\ s \tag{44}$$

generated by the optical source, eq 42, gives for $J = \mathrm{t}$, the triplet state population:

$$n_{\mathrm{t}}(\omega;\, T) = \frac{G_0\tau_1(T)}{1 + i\omega\tau_2(T)} \tag{45}$$

where the effective relaxation times τ_1 and τ_2 are defined as

$$\tau_1(T) = \frac{\tau_2(T)}{1 + f(T)} \tag{46}$$

and

$$\frac{1}{\tau_2(T)} \equiv \left(\frac{1}{1 + f(T)}\right)\left\{\left[\frac{1}{\tau_{\mathrm{Rt}}} + \frac{f(T)}{\tau_{\mathrm{Rs}}}\right] + \left[\frac{1}{\tau_{\mathrm{NRt}}(T)} + \frac{f(T)}{\tau_{\mathrm{NRs}}(T)}\right]\right\} \tag{47}$$

Here $f(T) \equiv (g_{\mathrm{s}}/g_{\mathrm{t}})\ \mathrm{e}^{-\Delta E/k_{\mathrm{B}}T}$ and $R_{\mathrm{st}} \equiv g_{\mathrm{s}}/g_{\mathrm{t}}$ is the degeneracy ratio (equals 1/3 in the singlet−triplet case).

Equation 47 is a statement that the total decay rate out of the split-energy state is equal to the sum of the radiative and nonradiative rates:

$$\frac{1}{\tau_2(T)} = \frac{1}{\tau_{\mathrm{R}}(T)} + \frac{1}{\tau_{\mathrm{NR}}(T)} \tag{48}$$

where

$$\tau_{\mathrm{R}}(T) = \tau_{\mathrm{Rt}}\left[\frac{1 + (g_{\mathrm{s}}/g_{\mathrm{t}})\ \mathrm{e}^{-\Delta E/k_{\mathrm{B}}T}}{1 + (g_{\mathrm{s}}/g_{\mathrm{t}})(\tau_{\mathrm{Rt}}/\tau_{\mathrm{Rs}})\ \mathrm{e}^{-\Delta E/k_{\mathrm{B}}T}}\right] \tag{49a}$$

and

$$\tau_{\mathrm{NR}}(T) = \tau_{\mathrm{NRt}}(T)\left[\frac{1 + (g_{\mathrm{s}}/g_{\mathrm{t}})\ \mathrm{e}^{-\Delta E/k_{\mathrm{B}}T}}{1 + (g_{\mathrm{s}}/g_{\mathrm{t}})(\tau_{\mathrm{NRt}}(T)/\tau_{\mathrm{NRs}}(T))\ \mathrm{e}^{-\Delta E/k_{\mathrm{B}}T}}\right] \tag{49b}$$

The radiative lifetime, eq 49a, was first derived independently by Calcott et al.[39] for Si nanocrystals; it has subsequently been used to represent the thermal equilibrium radiative lifetime of excitons both in Si nanocrystals[40] and in PbS nanocrystals in silicate glass.[22] Espiau de Lamaestre et al.[22] measured $\tau_{\mathrm{Rt}}/\tau_{\mathrm{Rs}} = 18 \pm 2$ (1.4 μm emission wavelength) and $\tau_{\mathrm{Rt}}/(\tau_{\mathrm{Rs}} = 5.2 \pm 0.4$ (1.6 μm emission wavelength). They also measured $\Delta E = 37 \pm 3$ meV (1.4 μm) and $\Delta E = 22 \pm 2$ meV (1.6 μm). For PbS in glass Gaponenko et al.[23] set

$$\Delta E = (m - n)E_{\mathrm{p}} \tag{50}$$

and using the LO-phonon energy $E_{\mathrm{P}} = 26.6$ meV, they found from transient PL that $\Delta E = (0.82 \pm 0.10) \times 26.6$ meV$= 21.8 \pm 3.2$ meV. Equation 49a was used without considering the degeneracy ratio. Furthermore, they normalized the radiative decay channel contribution to the maximum PL intensity value, thereby neglecting effective nonradiative lifetime contributions at lower temperatures. Yet, the frequency-domain PCR dynamic theory predicts such contributions concurrently with radiative decay channels, eq 49b) at all temperatures. There has been no prior expression for the nonradiative relaxation time such as the one derived in eq 49b, accounting for transitions between the singlet and triplet states through intermediate interactions with adjacent trap states. The nonradiative recombination lifetime in Si nanocrystals has been considered to involve multiphonon transition processes for trapping into deep centers[33] and an expression for $\tau_{\mathrm{NR}}(T)$ was derived using multiphonon theory.[41] Those expressions were not derived consistently with other relaxation pathways within a multichannel de-excitation manifold, such as is the case with PbS CQDs.

Using eqs 43, we can set in eq 49b

$$\frac{\tau_{\mathrm{NRt}}(T)}{\tau_{\mathrm{NRs}}(T)} = \left[\exp\left(\frac{E_{\mathrm{p}}}{k_{\mathrm{B}}T}\right) - 1\right]^{m-n} \tag{51}$$

From eqs 41a−41c we also find the singlet state population for $J = s$:

$$n_{\mathrm{s}}(\omega;\, T) = \frac{G_0 f(T)\tau_1(T)}{1 + i\omega\tau_2(T)} \tag{52}$$

Therefore, the total exciton population and density decaying from the split level is

$$n(\omega;\, T) = \frac{G_0[1 + f(T)]\tau_1(T)}{1 + i\omega\tau_2(T)} = \frac{G_0\tau_2(T)}{1 + i\omega\tau_2(T)} \tag{53}$$

This is the key equation describing the frequency-domain photoluminescence (excitonic PCR) signal as a function of the total system decay time constant τ_2, eq 47.

3. MATERIALS AND EXPERIMENTAL METHODS

For the purpose of probing excitonic carrier transport properties in QDs, two PbS CQD samples were fabricated and studied.[8,42] Both thin-film samples contained PbS colloidal quantum dots with mean diameter of 4.2 nm.The first ("uncoupled") sample was fabricated through drop casting of oleic acid capped PbS QDs. The large interparticle spacing of 4.2 nm does not allow strong interactions between dots, and hence the QDs were uncoupled. The second ("coupled") sample was fabricated through a layer-by-layer process in which the long oleic acid ligands were displaced by shorter 3-mercaptopropionic acid ligands, resulting in an interparticle spacing of about 0.5−1 nm. Such spacings allow for strong interactions between dots resulting in a coupled QD system.

The schematic diagram of the PCR experimental set-up, which was similar to our previous publications,[28] is shown in Figure 2. A 10 mW diode laser of 830 nm wavelength and a beam diameter of ca. 0.1 mm was square-wave modulated with a function generator. A 1 μm long-pass filter was placed in front of the InGaAs photodetector to block the excitation beam. No short-pass filter was necessary because thermal infrared contributions to the signal were found to be negligible. The sample was placed on a Linkam LTS350 cryogenic stage, which allows maintenance of constant temperature in the 77−520 K range. Since high temperatures would dramatically and irreversibly change the properties of the PbS CQDs, the highest temperature for frequency and temperature scans was set to 300 K.

4. RESULTS AND DISCUSSION

4.1. Radiative Relaxation Lifetime (Time-Resolved) Spectra.

Figure 3 shows the frequency-scanned PCR amplitude and phase responses. For both samples, decreasing temperature leads to pronounced growth of the PCR amplitude because of decreased nonradiative recombination probability at lower temperatures, which scales with phonon population as

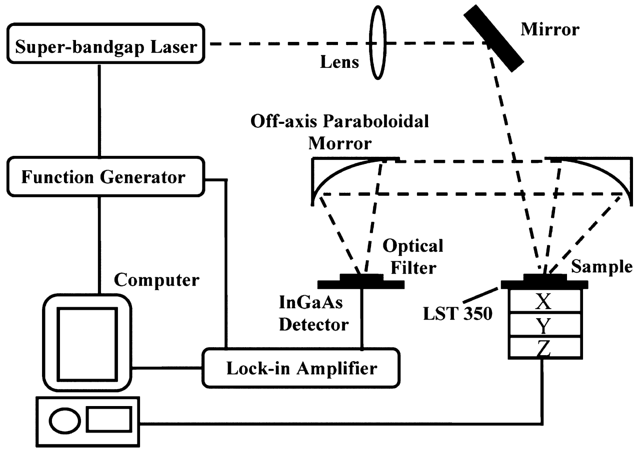

Figure 2. Schematic diagram of the photocarrier radiometry (PCR) setup for CQD frequency and temperature scans.

shown below (Figures 6 and 8). Similar trends in spectrally integrated transient PL intensity emitted by PbS QDs in glass have been observed by Gaponenko et al.[23] The larger high-frequency PCR phase lag with decreasing temperature is consistent with increased de-excitation lifetimes, again in agreement with the transient PL results in PbS in glass[23] and in Si NC.[40]

Two discrete-lifetime approaches were used, and each one involves two best-fitted data sets: lock-in amplitude and phase channel for the *ad hoc* discrete distribution model and real (in-phase) and imaginary (quadrature) channel for the variational inverse distribution model. With respect to the continuous lifetime-broadened Voigt integrals, with numerical calculations for eqs 7a and 7b, the PCR amplitude and phase signals for the uncoupled sample were fitted to the frequency-scan data with excellent agreement: the amplitude curves (#1) in Figure 3a and the phase curves (#1) were best-fitted to eqs 7a and 7b, so that

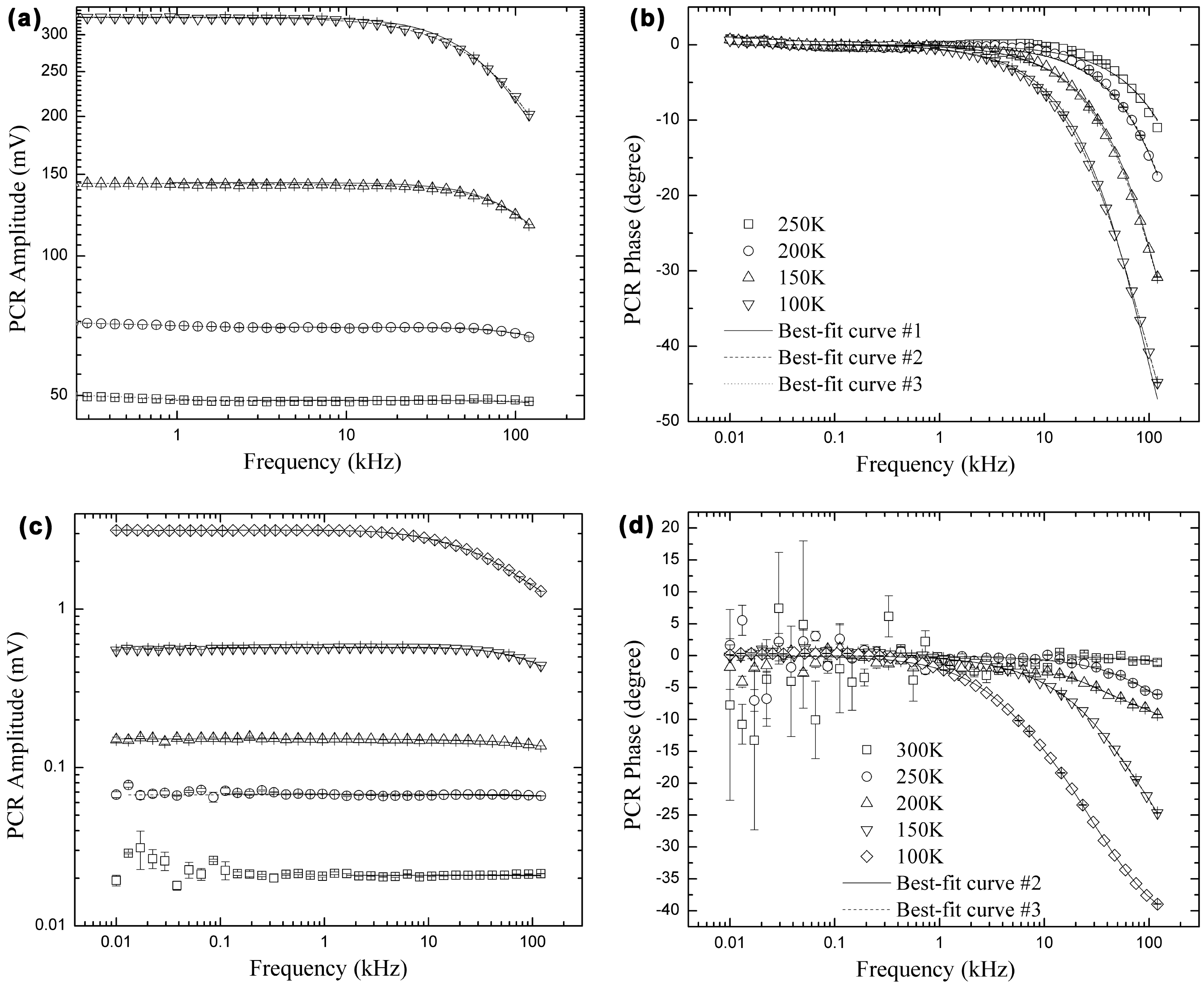

Figure 3. PCR frequency-scan spectra of the uncoupled and coupled samples at various temperatures. Best fitted curves #1 were calculated from eq 5, curves #2 from eq 11, and curves #3 from eqs 36 and 38. (a) Experimental amplitudes for the uncoupled sample; (b) phases for the uncoupled sample; (c) amplitudes for the coupled sample; (d) phases for the coupled sample. Error bars, when not apparent, are of the size of, or smaller than, the symbols.

Table 1. Fitted Lifetime (μs) Results of Phase Channel and Quadrature Channel at Various Temperatures (T) for the Uncoupled Sample

	continuous broadened lifetime (phase)					
T (K)	τ_0	$\Delta\tau$	τ_{ph}	τ_{pm}	τ_{ih}	τ_{im}
250	0.21	0.1 ± 0.05	0.24 ± 0.001	0.24 ± 0.001	0.08 ± 0.01	0.08 ± 0.02
200	0.4	0.1 ± 0.05	0.41 ± 0.001	0.41 ± 0.001	0.21 ± 0.01	0.20 ± 0.01
150	0.73 ± 0.02	0.4 ± 0.1	0.81 ± 0.02	0.87 ± 0.01	0.99 ± 0.005	0.99 ± 0.001
100	1.4 ± 0.01	0.7 ± 0.1	0.89 ± 0.03	1.68 ± 0.02	1.33 ± 0.02	1.88 ± 0.03

$$S(\omega) = \sqrt{A^2(\omega) + B^2(\omega)} \tag{54a}$$

$$\phi(\omega) = \tan^{-1}\left[\frac{B(\omega)}{A(\omega)}\right] \tag{54b}$$

The values of τ_0 (most probable decay lifetime) and broadening $\Delta\tau$ (statistical lifetime bandwidth) of eq 1 are shown in Table 1(Corresponding results for the amplitude channel are included in Supporting Information 2, Table 1). Using the experimental error bars shown in Figure 3, we also fitted the maximum and minimum of the standard deviations, and this resulted in the variances shown in Tables 1 and 4 for both samples with three fitting approaches. The small error bars show that our PCR method produces stable and precise lock-in signals. The most probable lifetime values lie between 0.2 and 1.4 μs in the range 100−300 K. These values are in very good agreement with the mean lifetime values measured for PbS QDs in glass[23] and with the room-temperature fluorescence lifetime in PbSe CQDs (0.88 μs).[10,13] The statistical lifetime bandwidth $\Delta\tau$ is roughly of the same order of magnitude as the most probable lifetime τ_0 at all temperatures, which is indicative of the large inhomogeneity in de-excitation rates in the uncoupled sample (likely due to temperature-dependent broad multienergetic excitonic trap distributions), superposed on much narrower homogeneous broadening due to temperature-independent QD size distribution. This is consistent with the Voigt response arising from a combination of inhomogeneous and homogeneous broadening.

In the case of the coupled sample with shorter inter-QD distance, the same Voigt-function procedure was attempted but could not yield good fits to the PCR signals, especially the phase at $T < 250$ K, so it was abandoned. The PCR phase is known to be more sensitive than the amplitude to the details of relaxation times associated with luminescent (radiative) emission processes in optoelectronic systems.[26,28] Therefore, it is concluded that a simple Voigt distribution is not appropriate to approximate the more complicated exciton de-excitation mechanism(s) for the coupled QD case. This might be expected from the fact that stronger interactions among nearest and possibly more remote neighbors are possible,[20] which are inconsistent with the QD local random distribution of radiative emissions implied in the Gaussian profile of eqs 1 and 5. On the other hand, the *ad hoc* discrete multidecay profile of eq 11 and the variational approach involve no a-priori assumptions with respect to exciton isolation and allow for the possibility of several independent, perhaps artificial, de-excitation modes, thereby implying exciton−exciton interactions, the likely result of the decreased interexcitonic distance. Using eq 11, we generated a best-fit algorithm and applied it to the experimental data of Figure 3c,d, labeled “best-fit curve #2”. A similar variational best-fit algorithm was generated using eqs 36 and 39 and was labeled “best-fit curve #3”. Best-fitting using the Voigt function was done by manually sweeping τ_0 and $\Delta\tau$ and building the spectra asymptotically with each successive sweep using $f(\tau) = f_0\ e^{-[(\tau-\tau_0)/\Delta\tau]^2}$ in eqs 7a and 7b until reasonable convergence was ensured. The result was the reconstruction of two normalized lifetime distributions. f_0 only affects the amplitude channel; however, the manual best-fit was applied to both amplitude and phase data after normalization ($f_0 = 1$), “best-fit curve #1” in Figure 3a,b.

The eq 11 best fits provided discrete multilifetime distributions or spectra τ_j weighed by probability factors f_j at each fixed temperature. In the present work, n was set to 70 to avoid information loss and the mean lifetime $\bar{\tau}$ was obtained by inserting (τ_1, τ_2, ..., τ_{70}) and (f_1, f_2, ..., f_{70}) into eq 12 as fitting parameters. Because of the random initial values generated by the program, the final best-fit results were not strictly unique; however, they produced similar $\bar{\tau}$ spectra. $\bar{\tau}$ values (named τ_{amp} and τ_{pha} for best-fitted amplitude and phase frequency scans, respectively) and the associated uncertainties were obtained by performing the calculation several times. The results are shown in Table 2. These results suggest that, while both amplitude and phase signals reflect the temperature dependence of exciton relaxation times, the phase signals with maximum variance 0.01% (uncoupled) and 0.43% (coupled) exhibit considerably higher SNR and thus yield much better resolved lifetime values than amplitudes. They represent the optimal precision of the PCR method, which thus proves to be much superior to transient PL derived lifetime values with typical uncertainty range 1.7−17%.[23,40] The very small phase variances carry important lifetime reconstruction reliability and resolution implications, and phase-generated lifetime spectra will be used exclusively for analysis in what follows, unless there are features in amplitudes that aid data interpretation. Figures 4 and 5 show the entire set of reconstructed lifetime spectra from phase (or quadrature) channel fitting results for both samples at several temperatures using all three methodologies (corresponding results for the amplitude (or in-phase) channel are included in Supporting Information 2, Figures 1 and 2). Figures 4b and 5a show the *ad hoc* reconstructed lifetime distributions. Although 70 lifetime values were produced for each curve, those with weighting constant $f_i < 0.1f_{max}$ were neglected. The dominant lifetime (the highest peak in each distribution) increases with

Table 2. Mean Lifetime (μs) and the Variance (a%) Calculated from the *ad Hoc* Discrete Multiple Decay Model

	uncoupled sample				coupled sample			
T (K)	τ_{pha}	a%	τ_{amp}	a%	τ_{pha}	a%	τ_{amp}	a%
300					0.06	0.25	0.15	5.90
250	0.24	0	0.42	5.04	0.23	0.43	0.24	4.99
200	0.41	0	0.74	1.77	0.80	0.11	0.82	7.78
150	0.87	0.01	1.10	5.51	1.34	0.03	0.95	5.35
100	1.68	0.01	2.03	0.57	5.85	0.04	5.66	2.65

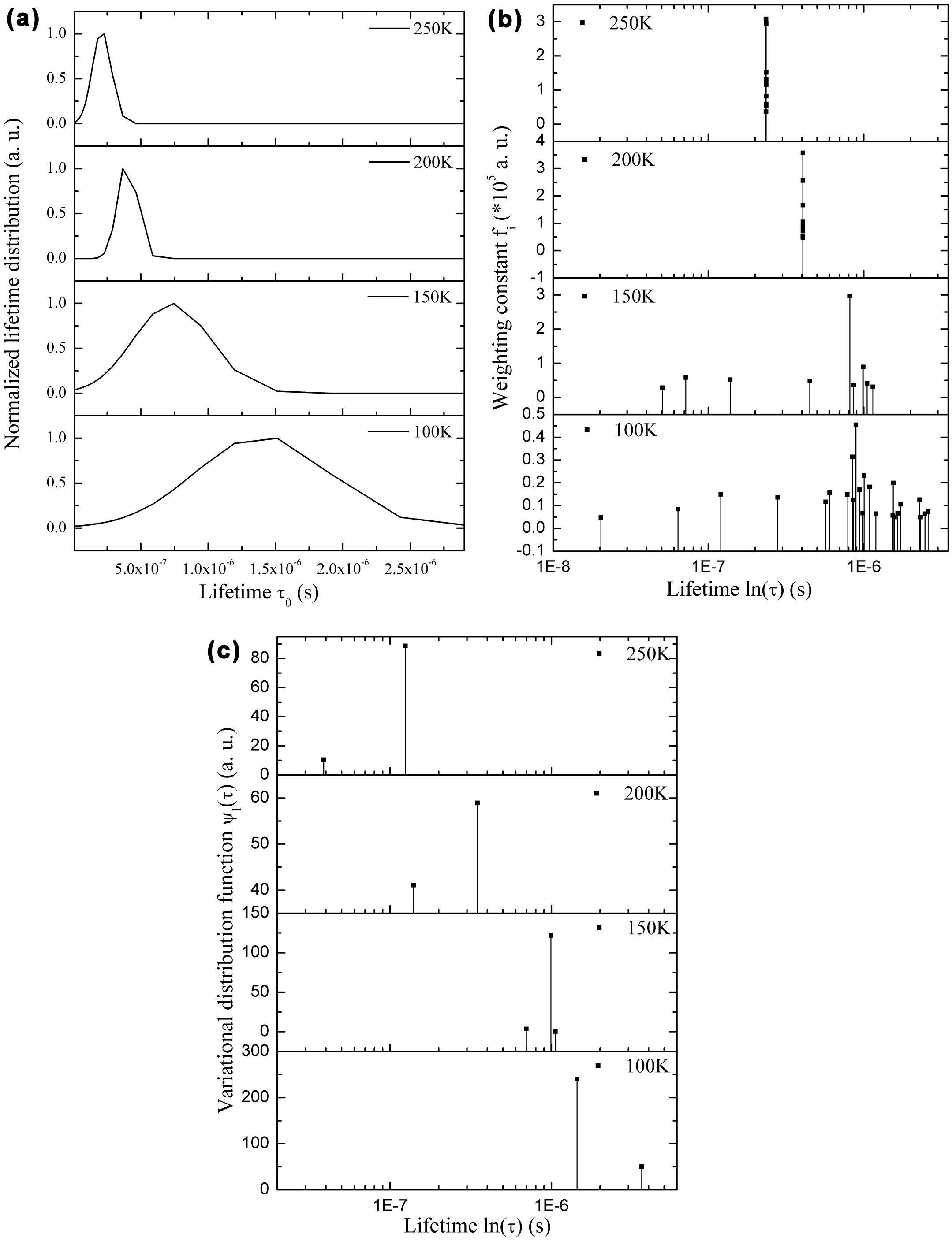

Figure 4. Continuous and discrete exciton lifetime distribution spectra of the uncoupled sample at various temperatures reconstructed from PCR frequency scan lock-in data: (a) continuous Voigt lifetime distribution from phase signal; (b) *ad hoc* discrete multiple lifetime distribution from phase signal; (c) variational discrete lifetime distribution from quadrature signal.

decreasing temperature, a clear trend for the uncoupled sample, which is consistent with the peaks of the continuous Voigt distribution, eq 5 and Figure 4a. However, the trend is more complicated for the coupled sample due to the large dispersion of the line spectra.

The variational inverse distribution model resulting in "best-fit curve #3", Figure 3, is based on the real and imaginary parts of the PCR signal. The best-fit results were recast into amplitude and phase channels

$$S(\omega) = \sqrt{F_R^{\,2}(\omega) + F_I^{\,2}(\omega)} \tag{55a}$$

$$\phi(\omega) = \tan^{-1}\left[\frac{F_I(\omega)}{F_R(\omega)}\right] \tag{55b}$$

Section 2.1.2.3, special case b, was used to reconstruct discrete lifetime spectra through matrix inversions, eqs 37 and 40, in order to compare the discrete variational and *ad hoc* multiple-lifetime distribution methods. Data fitting was done by setting ω_i $(1 \le i \le n)$ as the experimental angular frequencies

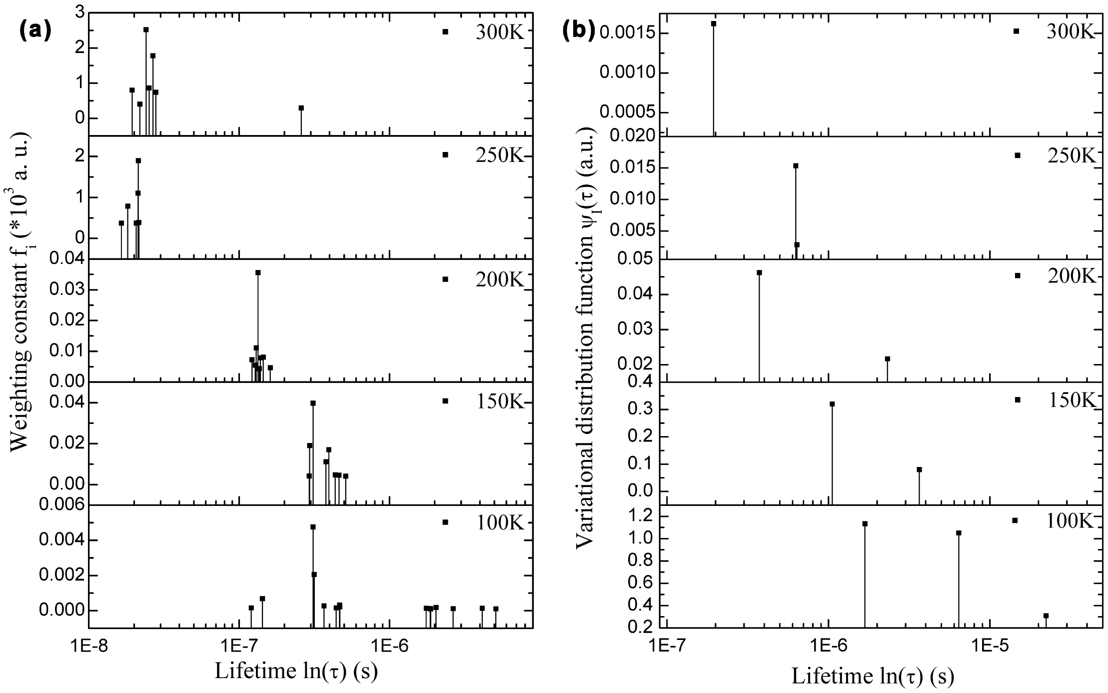

Figure 5. Continuous and discrete exciton lifetime distribution spectra of the coupled sample at various temperatures reconstructed from PCR frequency scan lock-in data: (a) *ad hoc* discrete multiple lifetime distribution from phase signal; (b) variational discrete lifetime distribution from quadrature signal.

(n equals the number of measured frequency points). The lifetime distributions on the time axis reconstructed from those matrix inversions correspond to the real (Supporting Information 2, Figures 1c and 2b) and imaginary parts and are shown in Figures 4c and 5b where line spectra with weighing function values $\Psi_{I/R}(\tau) < 10\%$ of Ψ_{max} were neglected, as was done with Figures 4b and 5a. These spectra exhibit similar trends in that the dominant lifetime increases when temperature decreases. However, the variational lifetime spectrum does not exhibit clustering around the dominant peaks. A comparison of the high-SNR variational and Voigt lifetime spectra of the uncoupled sample, Figure 4a,c, shows that strongly increased broadening with decreasing temperature is not accompanied by the emergence of clusters of additional variational peaks, unlike the *ad hoc* spectrum, but rather by a monotonic increase in the magnitude of the dominant peak as represented by the variational coefficient β_i in eqs 31 and 40 and a shift to longer lifetime values, consistent with the broadened profile. The Voigt phase spectral distribution full-width at half-maximum (fwhm) in Figure 4a was fitted to an exciton−phonon scattering model with the temperature-dependent LO phonon population controlling homogeneous lifetime broadening and an additional temperature-independent component accounting for inhomogeneous broadening:

$$\begin{aligned} \mathrm{fwhm}(T) &= \frac{\Delta\tau_0}{\langle n_P(T)\rangle} + \Delta\tau_I \\ &= \Delta\tau_0[\exp(E_P/k_BT) - 1] + \Delta\tau_I \end{aligned} \tag{56}$$

Figure 6 shows excellent results of the model's best-fit to the data. The calculated activation energy E_P = 22 meV is close to the known value of 26.6 meV in PbS nanocrystals in glass,[38] the difference also being justified in view of the different (colloidal) medium here. The best-fit value $\Delta\tau_I$ = 0.033 μs is small compared with the homogeneously broadened lifetime $\Delta\tau_0$ = 0.098 μs and mainly affects the fwhm at high T, while the effect of $\Delta\tau_0$ is more pronounced over the entire temperature range. $\Delta\tau_0$ is a measure of trap−exciton interaction distribution. Its relatively large value is consistent with the exciton−phonon interaction probability also involving excitonic decays into multienergetic trap or surface states. The conclusion here is that the dominant lifetime broadening mechanism over the 100−300 K temperature range in the uncoupled sample, a QD ensemble with long interdot distances, is homogeneous exciton−LO phonon scattering. Therefore, the lifetime

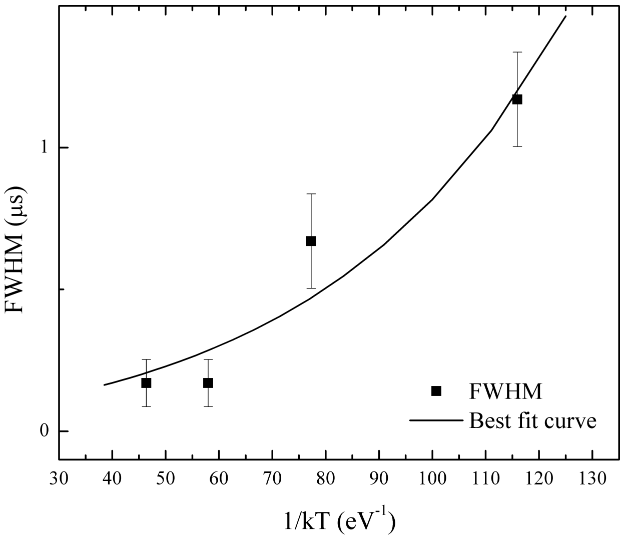

Figure 6. Plot of fwhm of the lifetime broadened spectrum of the uncoupled sample vs temperature dependence and best-fit to the homogeneous and inhomogeneous superposition model, eq 56. The fitting parameters are E_P = 22 meV, $\Delta\tau_0$ = 0.098 μs, and $\Delta\tau_I$ = 0.033 μs.

spectrum can be interpreted as the result of decreased exciton−phonon interactions with decreasing temperature (and phonon population), and a concomitant increase of the radiative emission rate (variational peak magnitude increase → luminescence photon flux increase, Figure 5c), accompanied by a decrease in the nonradiative rate when radiative lifetime becomes rate-limiting (shorter). In view of Figure 6, the narrow Voigt fwhm, Figure 4a at high temperatures, almost constant down to T = 200 K, represents a temperature-independent lifetime broadening limit, probably due to and a measure of, a relatively narrow nanoparticle size distribution in the sample as different size quantum dots are known to exist in all prepared ensembles.[11] The $T \geq 200$ K variational peak amplitude in Figure 4c, small compared with lower temperatures, is also consistent with low-probability radiative emissions. The high-temperature narrow fwhm is consistent with a very short mean scattering length, thereby promoting further isolation of the quantum dots from their immediate neighborhood. Exciton hopping,[43] which allows energy transfer from smaller dots to higher excited states of larger dots in a QD distribution such that larger dots exhibit longer decay lifetimes[11] within the framework of FRET mechanism, does not appear to affect the uncoupled sample. The appearance in the *ad hoc* spectra of multiple discrete peak distributions with decreasing temperature, accompanied by increased distribution spreading of the cluster away from the dominant peak, is probably an artifact of the reconstruction algorithm bereft of physical significance; however, it produces a magnitude envelope that is roughly consistent with the broadened Voigt profiles. It is important to note that the discretization of eq 4, which led to eq 11, is of limited τ resolution with a step of $\sim 0.5 \times 10^{-7}$ s, which does not satisfy the requirement $\sim 0.1 \times 10^{-7}$ s, the latter representing $\Delta\tau$ in the Voigt profile, Table 1. Nevertheless, the comparison in Tables 1and 2 between continuous and *ad hoc* mean discrete reconstructed lifetimes for the uncoupled sample shows that both sets of lifetime values are in good agreement with each other between 300 and 200 K, regardless of the model used. This agreement is consistent with the narrow Voigt fwhm centered on peak lifetime values τ_0 converging on the dominant spectral line, because there is no significant interaction between nearest neighbors due to LO phonon scattering lifetime dominance. Because the *ad hoc* peak clusters are only indicative of the lifetime spreads whereas the few variational peaks measure the most probable lifetime values, line spectra variances in the number of major reconstructed peaks are shown in Table 3 instead of the statistical variance of the mean lifetime in Table 2. When the number of the major peaks remained constant following repetitive execution of the reconstruction algorithm, the spectra variance was set to 0. The value of 1 means there is a deviation of one peak in the line spectrum. The observed excellent repeatability, Table 3, shows the high reliability of the variational inversion method.

Table 3. Number of Inverted Peaks (n) and Line Spectra Variance (SV) Calculated from the Discrete Variational Multiple Decay Model for Quadrature Channel

	uncoupled sample		coupled sample	
T (K)	n	SV	n	SV
300			1	0
250	1	0	1	0
200	1	0	2	0
150	2	0	2	1
100	2	0	3	0

For a thin film with a dense QD network of coupled CQDs, it is known that energy transfer from resonant energy states of smaller dots to higher excited states of larger dots in PbS dispersions is very efficient[11] and many nearest-neighbor-hopping (NNH) transitions occur at higher temperatures.[43] Table 2 shows that the coupled sample phase (or quadrature) extracted lifetime variance is much smaller than its amplitude- (or in-phase) extracted counterpart, as is also the case with the uncoupled sample. However, unlike the monotonic lifetime shifts of the major peak in the uncoupled case, here a degree of nonmonotonicity is observed as a result of the appearance of additional major lifetime components at low temperatures (≤200 K) in the variational quadrature spectrum. The inability to find an acceptable Voigt fit for the coupled sample at any temperature is indicative of the multiple de-excitation channel mechanism associated with simultaneous and independent energy decay pathways. Unlike the essentially self-confined uncoupled case, additional relaxation degrees of freedom in the coupled lifetime distribution profiles are likely to involve nearest neighbor inter-QD interactions in the form of excited state electron tunneling (NNH migration or a Förster resonance) and photon emission from another QD, with the main difference being a more complicated intersystem crossing network for the coupled sample and therefore wider lifetime line spectrum. These pathways manifest themselves as additional lifetime peaks at $T \leq 200$ K, Figure 5b. The much stronger increase of the radiative emission probability than its uncoupled counterpart as represented by the variational coefficients β_i in Figure 5b is also consistent with the shorter-range exciton−exciton interaction and the much higher probability of a hopping or tunneling exciton to enter the excited-state manifold of a neighboring quantum dot and decay or continue on to a tertiary excitonic site. Comparison between τ_{im} for the uncoupled case (single dominant lifetime) and the coupled case (mean of multiple lifetimes), Tables 1 and 4, shows that the ensemble with the shorter inter-QD distance (coupled case) consistently exhibits longer lifetimes, in agreement with the Förster radius theory, supporting the de-excitation energetics equivalence between single QDs of larger radii and QD clusters of short intra-QD distance.[44,45] This effect was previously observed in QD luminescence spectra only[11] and here it is corroborated by the lifetime spectra. It should be noted that in high QD density (coupled) thin-film structures, the short distance between adjacent QDs makes exciton hopping migration or FRET to nearby dots easier, which in turn leaves fewer carriers to recombine locally. As a result, the modulated PL intensity (PCR amplitude) of our coupled sample is much lower than that of the uncoupled sample, Figure 3a,c.

Table 4. Fitted Lifetime (μs) Results of Phase Channel and Quadrature Channel at Various Temperatures for the Coupled Sample

T (K)	τ_{ph}	τ_{pm}	τ_{ih}	τ_{im}
250	0.021 ± 0.003	0.23 ± 0.01	0.64 ± 0.05	0.786 ± 0.06
200	0.133 ± 0.001	0.8 ± 0.002	2.32 ± 0.3	1.13 ± 0.1
150	0.310 ± 0.01	1.34 ± 0.04	3.66 ± 0.1	1.83 ± 0.03
100	0.310 ± 0.03	5.85 ± 0.02	6.42 ± 0.1	6.58 ± 0.1

Table 5. Summary of Decay Parameters Fitted from Total Decay Rate Equation for the Uncoupled Sample and the Coupled Sample

	$\tau_2(T)$	τ_{NR0} (ns)	τ_{Rt} (μs)	τ_{Rs} (μs)	$m - n$	m	ΔE (meV)
uncoupled sample	τ_{pm}	235.2 ± 7	1.88 ± 0.01	0.006 ± 0.001	2.21 ± 0.01	7.78 ± 0.5	58.79 ± 0.3
	τ_{im}	2.8 ± 0.8	1.92 ± 0.03	1.69 ± 0.4	1.76 ± 0.3	3.53 ± 0.18	46.82 ± 7.9
	τ_{Vp}	27.6 ± 3	4.3 ± 1	0.065 ± 0.002	0.75 ± 0.11	2.99 ± 0.15	19.95 ± 2.9
coupled sample	τ_{pm}	0.06 ± 0.01	14.1 ± 2	0.015 ± 0.002	1.75 ± 0.1	10.69 ± 0.5	46.55 ± 2.7
	τ_{im}	0.01 ± 0.001	23.4 ± 1.2	0.039 ± 0.005	1.40 ± 0.03	17.54 ± 1.5	37.24 ± 0.8

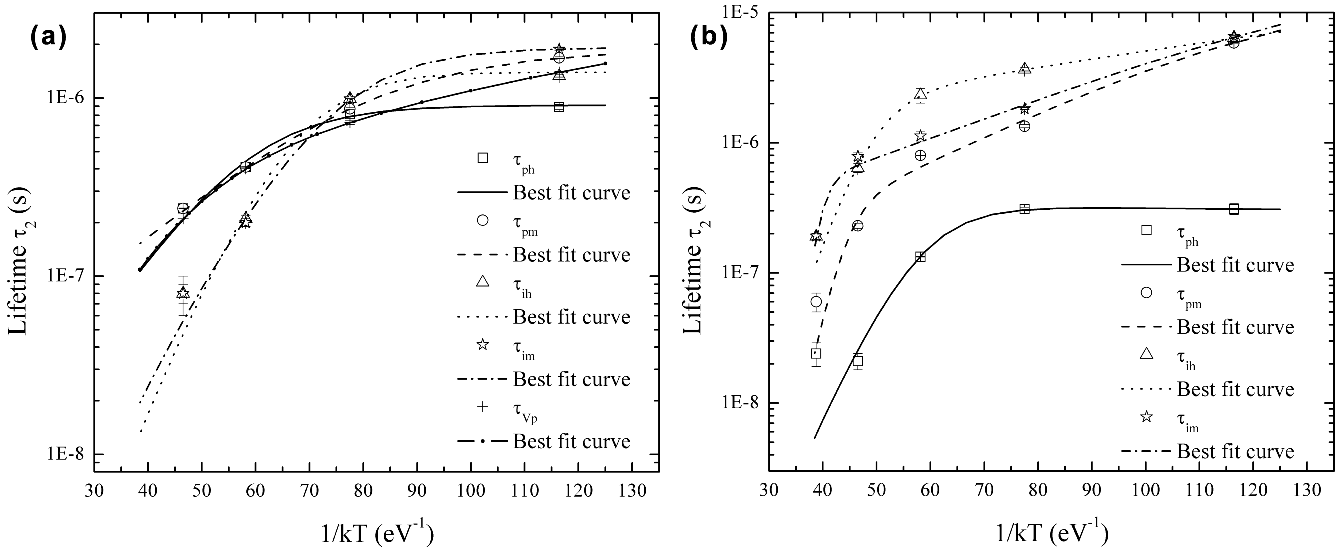

Figure 7. τ_2 vs $1/kT$. Lines are best-fitted curves with theory discussed in the text (eq 48). (a) the uncoupled case results; (b) the coupled case results.

4.2. Radiative and Nonradiative Lifetime Extraction and Temperature Dependencies. For mean lifetime calculations with the *ad hoc* discrete model, eq 12, parametric lifetimes were introduced. They are defined as τ_{ah}, τ_{am}, τ_{ph}, τ_{pm}, τ_{rh}, τ_{rm}, τ_{ih}, and τ_{im} and are shown in Table 1 for the uncoupled sample and in Table 4 for the coupled sample (τ_{ah}, τ_{am}, τ_{rh}, and τ_{rm} are shown in Supporting Information 2, Tables 1 and 2). These lifetime symbols stand for the highest magnitude and the mean lifetime values calculated from amplitude, phase, real part (in-phase) and imaginary part (quadrature) channel, respectively. The numerical results in Table 1for the uncoupled sample indicate that the two discrete methods produce similar temperature lifetime dependencies among all channels (phase, quadrature, amplitude and in-phase). Consistently with the lifetime spectra of Figures 4 and 5, the highest-peak and mean-lifetime values for the uncoupled sample, Table 1, are very close at all temperatures, an indication of one dominant radiative de-excitation mechanism. In contrast, the phase and quadrature highest and mean extracted values for the coupled sample are quite different below 250 K, indicating the emergence of multiple independent relaxation mechanisms.

The temperature dependence of lifetime on the exciton relaxation dynamics in QDs is described by eq 48. The temperature dependent lifetime values with highest reliability and accuracy, $\tau_{ph}(T)$, $\tau_{pm}(T)$, $\tau_{ih}(T)$, and $\tau_{im}(T)$, were successively set as the total decay lifetime, $\tau_2(T)$. Five parameters related to radiative and nonradiative relaxation, τ_{NR0}, τ_{Rt}, τ_{Rs}, $m - n$, and m, were fitted together; then the singlet−triplet state energy difference, ΔE, was calculated using eq 50. The results are shown in Table 5 for the uncoupled sample and the coupled sample (detailed results for $\tau_2(T)$ = $\tau_{ph}(T)$ and $\tau_{ih}(T)$ are shown in Supporting Information 2, Tables 3 and 4). Multiparameter best-fitting was performed with the Downhill Simplex method,[46] because there are many parameters and only finite sets of data; therefore, a fidelity prioritization of those parameters was introduced: it was found that the results for τ_{Rs}, $m - n$, and m are unique and precise. These three parameters determine the probable value of $\tau_2(T)$, while τ_{NR0} and τ_{Rt} affect the values of $\tau_2(T)$ to a lesser extent, near room temperature and at low temperatures, respectively. Table 5 also shows the results from the phase channel of the Gaussian-broadened Voigt distribution used to calculate τ_{Vp}. Using the variance in lifetime values, Table 1, variances of the parameters are also included in Table 5. Figure 7 shows Arrhenius plots of the five $\tau_2(T)$ functions from phase data with small variances of the mean lifetime derived from the experimental data.

To gain further insights into the origins of exciton relaxation physics, the total decay lifetime, $\tau_2(T)$, the radiative lifetime $\tau_R(T)$, and the nonradiative lifetime $\tau_{NR}(T)$ were calculated and compared. On the basis of our aforementioned conclusions about the SNR and repeatability advantages of phase and quadrature channels, the assumption $\tau_2(T) = \tau_{im}(T)$ was made, also because the variational phase and quadrature frequency responses conveniently exhibit self-normalization without a priori assumptions, in the form of zero value for all curves at low angular frequencies $\omega\tau_2(T) \ll 1$. This is an advantage over the assumption of zero nonradiative lifetime at low temperatures imposed by Gaponenko et al.[23] in order to normalize the radiative lifetime spectrum that they derived from pulsed photoluminescence data. The thus calculated parameters were then used to reconstruct $\tau_R(T)$ and $\tau_{NR}(T)$. The relative values

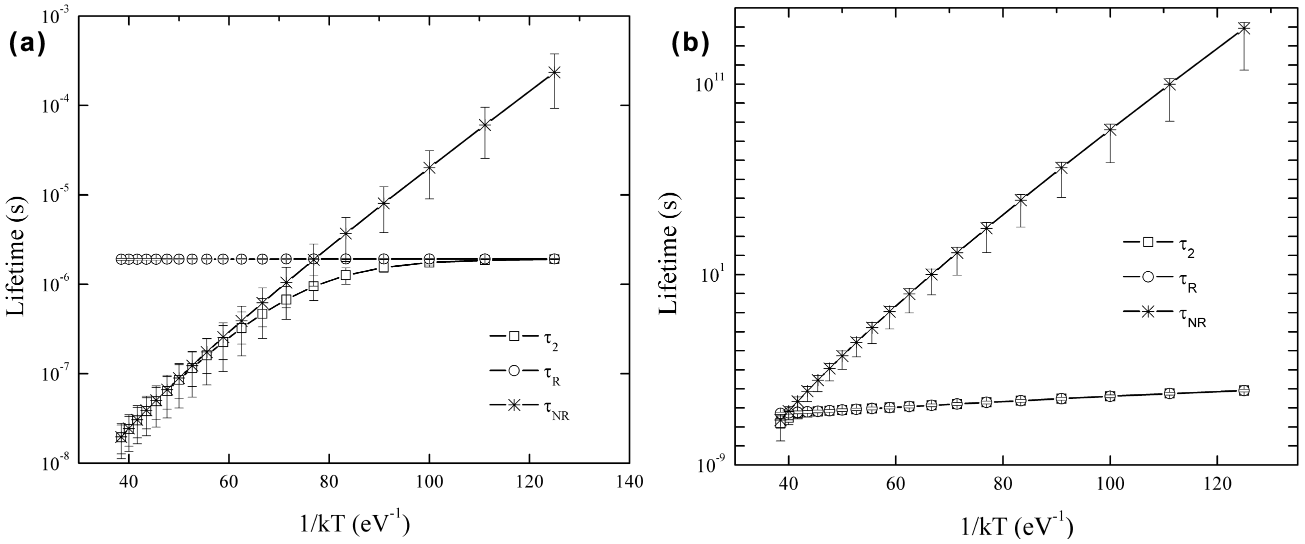

Figure 8. Best fitted curves of τ_2, τ_R, and τ_{NR} vs $1/kT$ for (a) the uncoupled sample and (b) the coupled sample.

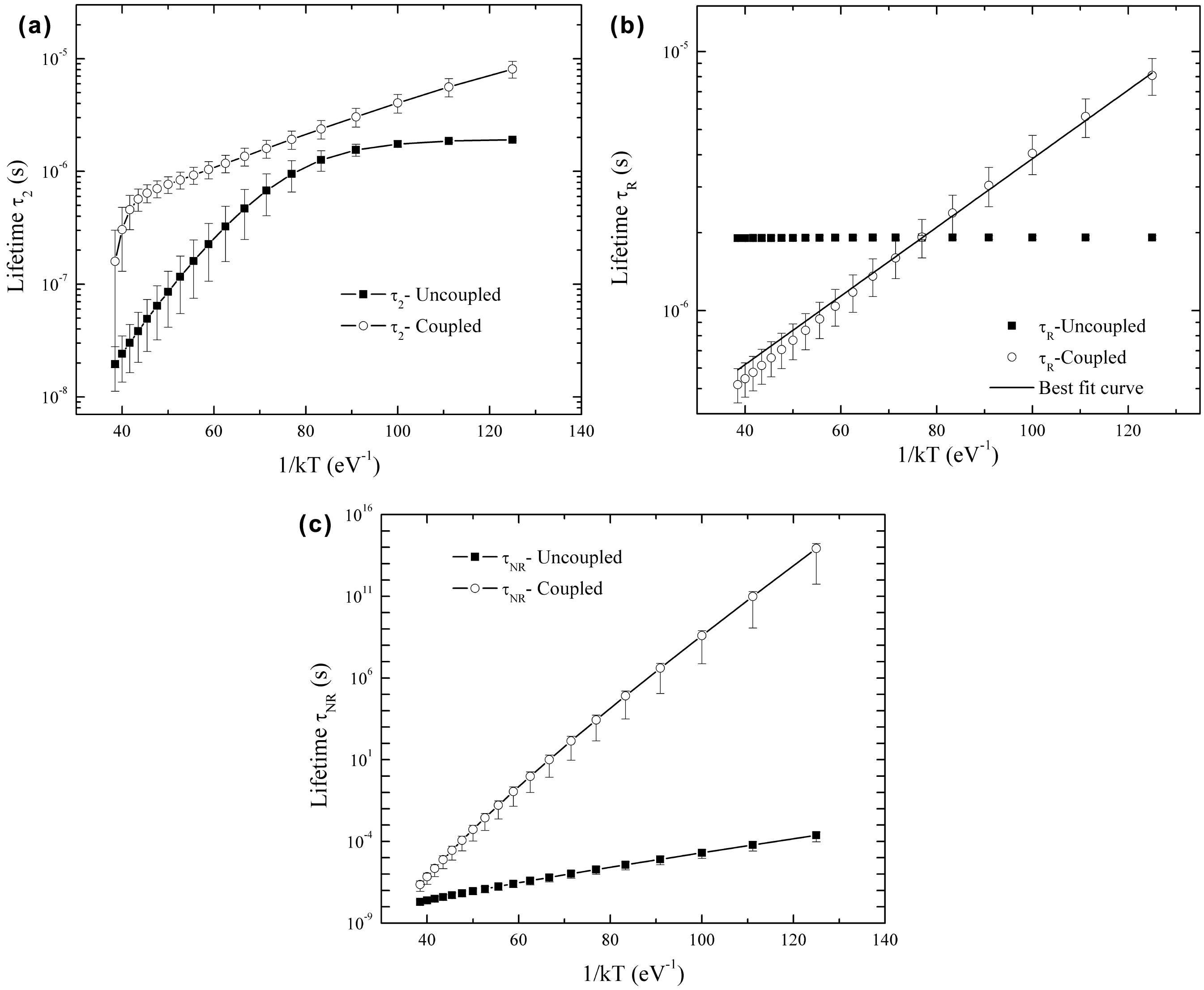

Figure 9. Best fitted Arrhenius curves for the uncoupled and coupled samples of (a) τ_2, (b) τ_R, and (c) τ_{NR}.

of $\tau_2(T)$ compared with $\tau_R(T)$ and $\tau_{NR}(T)$ for each sample are plotted in Figure 8.The reconstructed uncoupled case profiles in Figure 8a show that the $\tau_2(T)$ behavior is dominated by $\tau_{NR}(T)$ at high (up to room) temperatures, and it gradually converges to $\tau_R(T)$ as temperature decreases. On the other hand, $\tau_2(T)$ for the coupled case in Figure 8b is dominated by $\tau_R(T)$ almost across the entire temperature range from 100 to 300 K. The uncoupled sample trends in Figure 8a provide complementary information to the conclusions of the lifetime broadening profile, Figure 6: together they indicate that at relatively high temperatures, exciton−phonon scattering results in nonradiative relaxation stemming from the relative isolation of each exciton from the wider range of neighboring excitons due to large inter-QD distances. The exciton decay is assumed to be into multienergetic traps associated with the colloidal surroundings and surface states of the PbS nanoparticles, Figure 1. With decreased temperature, the phonon population also decreases. Exciton−phonon scattering leading to nonradiative de-excitation pathways, and phonon emission gradually ceases to dominate. In the presence of energetic exciton traps, it appears that phonon mediation is necessary for the nonradiative pathway to compete with radiative emissions. Additionally, the single-major-lifetime variational spectrum, Figure 4c, shows that in the uncoupled case the radiative relaxation mechanism is largely intra-QD, with all other lifetime decays contributing little or not at all, even at low T. This is also consistent with the monotonic lifetime shifts of the single dominant peak in Figure 4c.

The combination of variational and Voigt spectra in conjunction with the physical lifetime relaxation model of Figure 1 and section 2.2 point to a clear physical picture for the uncoupled case. The LO phonon−exciton interactions are radiative lifetime and luminescence photon flux (variational line spectrum peak strength) limiting throughout the entire 100−300 K temperature range. They are accompanied by phonon-mediated nonradiative exciton decay at high temperatures and a broadened inhomogeneous Voigt lifetime profile associated with the convolution of exciton−phonon interaction and, to a much lesser extent, temperature-independent factors such as QD size distribution. These conclusions are also consistent with but not obvious from the *ad hoc* discrete spectra, which exhibit no discernible trends in peak strength with temperature, albeit the dominant peaks show progressive dominant lifetime increases similar to the variational and Voigt spectra.

In the coupled sample with much shorter inter-QD distances, exciton tunneling or hopping and recombination degrees of freedom through extended distributions of neighboring QD excited-state manifolds dominates over almost the entire temperature range, Figure 8b, consistent with the NNH mechanism,[11] which operates independently from exciton−phonon-collision, nonradiative-decay-inducing processes. The gradual shift of radiative rate domination to inter-QD crossing as exciton−phonon scattering increases with increasing temperature thereby affecting the intra-QD radiative relaxation rate is consistent with the trends in the variational spectrum of Figure 5b, which shows two dominating lifetimes appearing for $T \leq$ 200 K. The emergence of the strong shorter lifetime peak occurs at the expense of the single dominant longer lifetime peak and possibly reflects increasing exciton NNH rates and decays from higher excited states of neighboring QDs of larger sizes than that in which the exciton originated.[11] It is interesting to note that the shorter low-temperature lifetime peak in Figure 5b, once it emerges, also grows in strength and shifts to longer values with further decreases in temperature. This is consistent with secondary and possibly higher-order phonon−exciton interactions following NNH among neighboring QDs. It can also be concluded that the appearance of the shorter lifetime peak marks the effective onset of excitonic hopping occurring from smaller to larger colloidal PbS QDs from which, in turn, excitons relax at faster rates than those in the original QD, also consistent with PbS QDs embedded in a Nafion membrane.[13]

Although the mean lifetime $\tau_2(T)$ has small variance due to the high SNR experimental results, the derived values of $\tau_R(T)$ and $\tau_{NR}(T)$ shown in Figure 8 and calculated from eq 49 with the fitting parameters in Table 5 are more sensitive to the original fitting lifetime values and exhibit larger variances. Figure 9 shows Arrhenius plots for the total $\tau_2(T)$ lifetime and its constituent lifetimes for the two samples. It is seen that $\tau_2(T)$ of the coupled sample is longer than that of the uncoupled sample at all temperatures, Figure 9a, as expected from the smaller impact of nonradiative decay channels and the added direct exciton-to-exciton degrees of freedom in the coupled case. The $\tau_R(T)$ of the coupled sample is a much more sensitive function of temperature than that in the uncoupled case, Figure 9b, exhibiting an approximately exponential increase with decreasing temperature. Figure 9b shows an exponential best-fit to the $\tau_R(T)$ curve extracted from the coupled sample lifetime data:

$$\tau_R(T) = \tau_{R0} \exp(E/(k_B T)) \tag{57}$$

The best-fit parameters are E = 30.5 meV and τ_{R0} = 0.183 μs. The activation energy is in good agreement with the value 37 meV for the interlevel energy spacing, ΔE, derived from the full fit to the data, Table 5, but higher than 21.8 ± 3.2 meV for PbS in glass.[23] The exponential fit is the result of the large τ_{Rt}/τ_{Rs} = 23.4/0.039 ratio in eq 49a. This is consistent with the fact that the nonradiative recombination rate in the coupled sample is much lower than in the case of quasi-isolated excitons in the uncoupled sample, Figure 9c, and τ_R is therefore rate-limited through phonon scattering, the population of which decreases exponentially with decreasing temperature.

The foregoing uncoupled and coupled sample lifetime distribution behaviors can be further understood from the fact that the uncoupled sample is capped with oleic acid, an insulating ligand that prevents carriers from diffusing. The coupled sample on the other hand is capped with 3-mercaptopropionic acid, which brings the CQDs close together allowing carriers to diffuse or hop over a large number of CQDs likely involving shallow nonradiative states, which may be inefficient, low-occupation-probability photocarrier traps[45] that can be thermally emptied even at low temperatures. This increases the effective nonradiative lifetime, as shown in Figure 9c. The implication here is that such traps cannot be photocurrent-limiting recombination sites in a photovoltaic device configuration. Such a device based on coupled CQDs is expected to exhibit moderate mobilities and high short-circuit currents.[21]

5. CONCLUSIONS

The PCR method was applied for the first time to the study of optoelectronic properties of PbS CQDs with different interdot spacing. Using three lifetime relaxation models, we reconstructed lifetime distribution spectra from the PCR frequency-response data, and the temperature dependence of lifetimes was analyzed using an exciton manifold decay model involving radiative and nonradiative pathways. The high lock-in signal-to-noise ratio inherent in PCR allowed the generation of reliable continuous and discrete lifetime spectra and yielded physical mechanisms of intradot and interdot excitonic interactions. With this energetic exciton model and the reconstructed lifetime spectra, the lowest 1S−1S exciton splitting energy was determined to be 37 meV and the radiative and nonradiative lifetimes were calculated without any need for signal normalization at low temperatures. They were found to be 0.039 and 23.4 μs, respectively, for the singlet state, and 0.13 and 0.3 μs for the triplet state of a sample with small interdot distance used in the fabrication of CQD solar cells. The excitonic model together with the high-reliability of the variational lifetime line spectrum can be further used to identify the temperature threshold for the onset of NNH and exciton−exciton hopping interactions in coupled CQD systems.

■ ASSOCIATED CONTENT

Ⓢ Supporting Information

(1) Variational method for Fredholm integral equation solution and (2) part of fitting results of the uncoupled and coupled sample. This material is available free of charge via the Internet at http://pubs.acs.org.

■ AUTHOR INFORMATION

Corresponding Author

*Phone: 001-(416)-978-1287. Fax: 001-(416)-266-7867. E-mail: mandelis@mie.utoronto.ca.

Notes

The authors declare no competing financial interest.

■ ACKNOWLEDGMENTS

A. Mandelis is grateful to the Natural Sciences and Engineering Research Council (NSERC) for a Discovery grant, to the Canada Foundation for Innovation (CFI) for equipment grants, to the Canada Research Chairs Program, and to the Ontario Ministry for Research and Innovation (MRI) for the Inaugural Premier's Discovery Award in Science and Technology (2007). J. Wang is grateful to the China Scholarship Council (CSC) for an international student grant.

■ REFERENCES

(1) Clifford, J. P.; Konstantatos, G.; Johnston, K. W.; Hoogland, S.; Levina, L.; Sargent, E. H. Fast, Sensitive and Spectrally Tunable Colloidal-quantum-dot Photodetectors. *Nat. Nanotechnol.* **2009**, *4*, 40−44.

(2) Konstantatos, G.; Howard, I.; Fischer, A.; Hoogland, S.; Clifford, J. P.; Klem, E.; Levina, L.; Sargent, E. H. Ultrasensitive Solution-cast Quantum dot Photodetectors. *Nature* **2006**, *442*, 180−183.

(3) Coe, S.; Woo, W. K.; Bawendi, M.; Bulovic, V. Electroluminescence from Single Monolayers of Nanocrystals in Molecular Organic Devices. *Nature* **2002**, *420*, 800−803.

(4) Mueller, A. H.; Petruska, M. A.; Achermann, M.; Werder, D. J.; Akhadov, E. A.; Koleske, D. D.; Hoffbauer, M. A.; Klimov, V. I. Multicolor Light-Emitting Diodes Based on Semiconductor Nanocrystals Encapsulated in GaN Charge Injection Layers. *Nano Lett.* **2005**, *5*, 1039−1044.

(5) Johnston, K. W.; Pattantyus-Abraham, A. G.; Clifford, J. P.; Myrskog, S. H.; MacNeil, D. D.; Levina, L.; Sargent, E. H. Schottky-quantum dot Photovoltaics for Efficient Infrared Power Conversion. *Appl. Phys. Lett.* **2008**, *92*, No. 151115.

(6) McDonald, S. A.; Konstantatos, G.; Zhang, S.; Cyr, P. W.; Klem, E. J. D.; Levina, L.; Sargent, E. H. Solution-processed PbS Quantum dot Infrared Photodetectors and Photovoltaics. *Nat. Mater.* **2005**, *4*, 138−142.

(7) Maraghechi, P.; Labelle, A. J.; Kirmani, A. R.; Lan, X.; Adachi, M. M.; Thon, S. M.; Hoogland, S.; Lee, A.; Ning, Z.; Fischer, A.; Amassian, A.; Sargent, E. H. The Donor Supply Electrode Enhances Performance in Colloidal Quantum Dot Solar Cells. *ACS Nano* **2013**, *7*, 6111−6116.

(8) Pattantyus-Abraham, A. G.; Kramer, I. J.; Barkhouse, A. R.; Wang, X.; Konstantatos, G.; Debnath, R.; Levina, L.; Raabe, I.; Nazeeruddin, M. K.; Grätzel, M.; Sargent, E. H. Depleted-Heterojunction Colloidal Quantum Dot Solar Cells. *ACS Nano* **2010**, *4*, 3374−3380.

(9) Mentzel, T. S.; Porter, V. J.; Geyer, S.; MacLean, K.; Bawendi, M. G.; Kastner, M. A. Charge Transport in PbSe Nanocrystal Arrays. *Phys. Rev. B* **2008**, *77*, No. 075316.

(10) Kang, M. S.; Sahu, A.; Norris, D. J.; Frisbie, C. D. Size- and Temperature-dependent Charge Transport in PbSe Nanocrystal Thin Films. *Nano Lett.* **2011**, *11*, 3887−3892.

(11) Clark, S. W.; Harbold, J. M.; Wise, F. W. Resonant Energy Transfer in PbS Quantum Dots. *J. Phys. Chem. C* **2007**, *111*, 7302−7305.

(12) Chen, Y.; Yu, D.; Li, B.; Chen, X.; Dong, Y.; Zhang, M. Size-dependent Radiative Emission of PbS Quantum dots Embedded in Nafion Membrane. *Appl. Phys. B: Laser Opt.* **2009**, *95*, 173−177.

(13) Wehrenberg, B. L.; Wang, C.; Guyot-Sionnest, P. Interband and Intraband Optical Studies of PbSe Colloidal Quantum Dots. *J. Phys. Chem. B* **2002**, *106*, 10634−10640.

(14) Lifshitz, E.; Sirota, M.; Porteanu, H. Continuous and Time-resolved Photoluminescence Study of Lead Sulfide Nanocrystals, Embedded in Polymer Film. *J. Cryst. Growth* **1999**, *196*, 126−134.

(15) Yu, P.; Nedeljkovic, J. M.; Ahrenkiel, P. A.; Ellingson, R. J.; Nozik, A. J. Electronic Coupling in InP Nanoparticle Arrays. *Nano Lett.* **2003**, *3*, 169.

(16) Romero, H. E.; Drndic, M. Coulomb Blockade and Hopping Conduction in PbSe Quantum Dots. *Phys. Rev. Lett.* **2005**, *95*, No. 156801.

(17) Talapin, D. V.; Lee, J. S.; Kovalenko, M. V.; Shevchenko, E. V. Prospects of Colloidal Nanocrystals for Electronic and Optoelectronic Applications. *Chem. Rev.* **2010**, *110*, 389−458.

(18) Ellingson, R. J.; Beard, M. C.; Johnson, J. C.; Yu, P. R.; Micic, O. I.; Nozik, A. J.; Shabaev, A.; Efros, A. L. Highly Efficient Multiple Exciton Generation in Colloidal PbSe and PbS Quantum Dots. *Nano Lett.* **2005**, *5*, 865−871.

(19) Istrate, E.; Hoogland, S.; Sukhovatkin, V.; Levina, L.; Myrskog, S.; Smith, W. E.; Sargent, E. H. Carrier Relaxation Dynamics in Lead Sulfide Colloidal Quantum Dots. *J. Phys. Chem. B* **2008**, *112*, 2757−2760.

(20) Konstantatos, G.; Sargent, E. H. PbS Colloidal Quantum Dot Photoconductive Photodetectors: Transport, Traps, and Gain. *Appl. Phys. Lett.* **2007**, *91*, No. 173505. Zhitomirsky, D.; Voznyy, O.; Hoogland, S.; Sargent, E. H. Measuring Charge Carrier Diffusion in Coupled Colloidal Quantum Dot Solids. *ACS Nano* **2013**, *7*, 5282−5290.

(21) Gao, J.; Johnson, J. C. Charge Trapping in Bright and Dark States of Coupled PbS Quantum Dot Films. *ASC Nano* **2012**, *6*, 3292−3303.

(22) Espiau de Lamaestre, R.; Bernas, H.; Pacifici, D.; Franzo, G.; Priolo, F. Evidence for a "Dark Exciton" State of PbS Nanocrystals in a Silicate Glass. *Appl. Phys. Lett.* **2006**, *88*, No. 181115.

(23) Gaponenko, M. S.; Lutich, A. A.; Tolstik, N. A.; Onushchenko, A. A.; Malyarevich, A. M.; Petrov, E. P.; Yumashev, K. V. Temperature-dependent Photoluminescence of PbS Quantum Dots in Glass: Evidence of Exciton State Splitting and Carrier Trapping. *Phys. Rev. B* **2010**, *82*, No. 125320.

(24) Batista, J.; Mandelis, A.; Shaughnessy, D. Temperature Dependence of Carrier Mobility in Si Wafers Measured by Infrared Photocarrier Radiometry. *Appl. Phys. Lett.* **2003**, *82*, 4077−4079.

(25) Mandelis, A.; Batista, J.; Shaughnessy, D. Infrared Photocarrier Radiometry of Semiconductors: Physical principles, Quantitative Depth Profilometry, and Scanning Imaging of Deep Subsurface Electronic Defects. *Phys. Rev. B* **2003**, *67*, No. 205208.

(26) Xia, J.; Mandelis, A. Direct-search Deep Level Photothermal Spectroscopy: An Enhanced Reliability Method for Overlapped Semiconductor Defect State Characterization. *Appl. Phys. Lett.* **2010**, *96*, No. 262112.

(27) Xia, J.; Mandelis, A. Radiative Defect State Identification in Semi-insulating GaAs using Photo-carrier Radiometry. *Semicond. Sci. Technol.* **2009**, *24*, No. 125002.

(28) Xia, J.; Mandelis, A. Broadening Effects and Ergodicity in Deep Level Photothermal Spectroscopy of Defect States in Semi-insulating GaAs: A Combined Temperature-, Pulse-rate-, and Time-domain Study of Defect State Kinetics. *J. Appl. Phys.* **2009**, *105*, No. 103712.

(29) Peterson, J. J.; Krause, T. D. Fluorescence Spectroscopy of Single Lead Sulfide Quantum Dots. *Nano Lett.* **2006**, *6*, 510−514.

(30) Sampoorna, M.; Nagendra, K. N.; Frisch, H. Generalized Voigt Functions and Their Derivatives. *J. Quant. Spectrosc. Radiat. Transfer* **2007**, *104*, 71−85.

(31) Palmer, R. G.; Stein, D. L.; Abrahams, E.; Anderson, P. W. Models of Hierarchically Constrained Dynamics for Glassy Relaxation. *Phys. Rev. Lett.* **1984**, *53*, 958−961.

(32) Kohlrausch, R. *Ann. Phys. (Leipzig)* **1847**, *12*, 393.

(33) Roman, H. E.; Pavesi, L. Monte Carlo Simulations of the Recombination Dynamics in Porous Silicon. *J. Phys.: Condens. Matter* **1996**, *8*, 5161−5187.

(34) Pavesi, L. Influence of Dispersive Exciton Motion on the Recombination Dynamics in Porous Silicon. *J. Appl. Phys.* **1996**, *80*, 216−225.

(35) Linnros, J.; Lalic, N.; Galeckas, A.; Grivickas, V. Analysis of the Stretched Exponential Photoluminescence Decay from Nanometer-sized Silicon Crystals in S_iO_2. *J. Appl. Phys.* **1999**, *86*, 6128−6134.

(36) O'Neil, M.; Marohn, J.; McLendon, G. Dynamics of Electron-Hole Pair Recombination in Semiconductor Clusters. *J. Phys. Chem.* **1990**, *94*, 4356−4363.

(37) Johnson, J. C.; Gerth, K. A.; Song, Q.; Murphy, J. E.; Nozik, A. J. Ultrafast Exciton Fine Structure Relaxation Dynamics in Lead Chalcogenide Nanocrystals. *Nano Lett.* **2008**, *8*, 1374−1381.

(38) Kraus, T. D.; Wise, F. W. Coherent Acoustic Phonons in a Semiconductor Quantum Dot. *Phys. Rev. Lett.* **1997**, *79*, 5102−5105.

(39) Calcott, P. D.; Nash, K. J.; Canham, L. T.; Kane, M. J.; Brumhead, D. Identification of Radiative Transitions in Highly Porous Silicon. *J. Phys.: Condens. Matter* **1993**, *5*, L91−L98;Calcott, P. D.; Nash, K. J.; Canham, L. T.; Kane, M. J.; Brumhead, D. Spectroscopic identification of the luminescence mechanism of highly porous silicon. *J. Lumin.* **1993**, *57*, 257−269.

(40) Heitmann, J.; Mueller, F.; Yi, L.; Zacharias, M.; Kovalev, D.; Eichorn, F. Excitons in Si Nanocrystals: Confinement and Migration Effects. *Phys. Rev. B* **2004**, *69*, No. 195309.

(41) Ridley, B. K. Multiphonon, Non-radiative Transition Rate for Electrons in Semiconductors and Insulators. *J. Phys. C: Solid State Phys.* **1978**, *11*, 2323−2341.

(42) Debnath, R.; Bakrbc, O.; Sargent, E. H. Solution-processed Colloidal Quantum Dot Photovoltaics: A Perspective. *Energy Environ. Sci.* **2011**, *4*, 4870−4881.

(43) Warner, J. H.; Thomsen, E.; Watt, A. R.; Heckenberg, N. R.; Rubinsztein-Dunlop, H. Time-Resolved Photoluminescence Spectroscopy of Ligand-capped PbS Nanocrystals. *Nanotechnology* **2005**, *16*, 175−179.

(44) Förster, T. 10th Spiers Memorial Lecture Transfer Mechanisms of Electronic Excitation. *Discuss. Faraday Soc.* **1959**, *27*, 7−17.

(45) Ip, A. H.; Thon, S. M.; Hoogland, S.; Voznyy, O.; Sargent, E. H. Hybrid Passivated Colloidal Quantum Dot Solids. *Nat. Nanotechnol.* **2012**, *7*, 577−582.

(46) Press,W. H.; Teukolsky, S. A.; Vetterling, W. T.; Flannery, B. P. *Numerical Recipes in Fortran*, 2nd ed.; Cambridge University Press: New York, 1992; Vol. *1*, pp 402−407.